

Near-Field Visualization of Strongly Confined Surface Plasmon Polaritons in Metal–Insulator–Metal Waveguides

Ewold Verhagen,^{*,†} Jennifer A. Dionne,[‡] L. (Kobus) Kuipers,[†] Harry A. Atwater,[‡] and Albert Polman[†]

Center for Nanophotonics, FOM Institute for Atomic and Molecular Physics, Kruislaan 407, 1098 SJ Amsterdam, The Netherlands, and Thomas J. Watson Laboratory of Applied Physics, California Institute of Technology, Pasadena, California 91125

Received June 20, 2008

ABSTRACT

A nanoscale gap between two metal surfaces can confine propagating surface plasmon polaritons (SPPs) to very small dimensions, but this geometry makes it inherently difficult to image SPP propagation at high resolution. We demonstrate the near-field probing of these SPPs, propagating within a 50 nm thick Si_3N_4 waveguide with Ag cladding layers for frequencies ranging from the blue to the near-infrared. Using near-field SPP interferometry, we determine the wave vector, showing that the wavelength is shortened to values as small as 156 nm for a free-space wavelength of 532 nm.

Much effort has been recently dedicated to controlling light propagation on the nanoscale using metal surfaces that support surface plasmon polaritons (SPPs). In dielectric media, the diffraction limit sets a lower bound to the size with which guided waves can be confined. This limit can be significantly reduced using SPPs, which are evanescent surface waves coupled to charge oscillations of the free electrons in the metal.^{1,2} The SPP wavelength is shorter than that of light, and modal fields are confined close to the metal surface. These effects are particularly strong for SPPs guided in a nanosized dielectric gap between two metals.^{3–5} Such a metal–insulator–metal (MIM) geometry serves as a plasmonic slot waveguide, “squeezing” the SPP field into the dielectric core. As a result, the wavelength along the direction of propagation is shortened significantly. MIM-SPPs can therefore be guided in waveguides with very small transverse dimensions⁶ and allow the realization of nanocavities with extremely small mode volumes.^{7,8} In comparison to other SPP guiding geometries, the cost of extra losses that are linked to the increase in confinement is relatively low.^{4,5,9} MIM-SPPs are responsible for the resonances in slits in metal films that lead to large field enhancements and large resonant transmission¹⁰ and are closely related to SPPs guided along grooves and slits in metal films.^{11,12} Furthermore, SPP modes in MIM geometries have been demonstrated to exhibit two-dimensional negative refraction in certain frequency regimes.¹³

In order to develop new nanostructured components that control the propagation of these waves, it is crucial to image their fields at the highest possible resolution and to study their propagation properties. It is therefore important to gain direct access to the near field of these modes. However, such imaging is inherently difficult because of the presence of the metal cladding. So far, experiments have been limited to spectral analysis of the far field reflection and transmission of finite length waveguides and cavities.^{6,7}

In this Letter, we present the near-field imaging and quantitative analysis of MIM-SPPs. By reducing the thickness of one of the metallic cladding layers of the slot waveguide, tunneling of light from a near-field probe to the highly confined SPP mode is demonstrated without negatively affecting the interesting properties associated with these waves. With the light scattered from subwavelength slits, interferometric measurements are performed that provide accurate in situ determination of the wave vector of SPP modes guided either in the MIM slot or in the air outside the sample. Excellent correspondence with calculated dispersion is obtained for frequencies ranging from the blue to the near-infrared. The smallest observed MIM-SPP wavelength is 156 nm, measured at a free-space wavelength of 532 nm.

A sketch of the experimental geometry is shown in Figure 1a. The sample consists of a 50 nm thick suspended Si_3N_4 membrane, coated on both sides with Ag by thermal evaporation. This design results in small interface roughness determined by the smoothness of the Si_3N_4 , which limits scattering losses. The Ag thickness on the front side of the sample is only 35 nm to allow for sufficient near-field

* Corresponding author, verhagen@amolf.nl.

† FOM Institute for Atomic and Molecular Physics.

‡ California Institute of Technology.

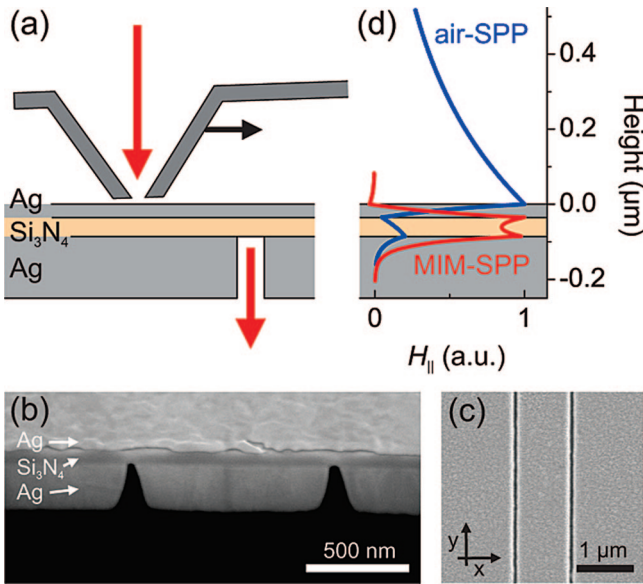


Figure 1. (a) Schematic depiction of the measurement geometry. Laser light is incident through the aperture of an Al near-field probe, which is scanned with respect to the sample. Light transported through the MIM waveguide is collected after scattering from subwavelength slits in the back Ag film. (b, c) SEM micrographs of the fabricated waveguide, shown in cross section (b) and as viewed from the bottom (c). The waveguide consists of 50 nm of Si₃N₄ clad with 35 nm of Ag on the top and 310 nm of Ag on the bottom. (d) H_{\parallel} field mode profiles of the two waveguided SPP modes supported by the multilayer stack.

coupling of a probe outside the sample to the dielectric core of the waveguide. The near-field probe is a hollow Al pyramid on a Si cantilever, with a tip aperture that has a diameter smaller than 100 nm (WITec GmbH). The thickness of the Al sidewalls of the probe is ~ 250 nm. Light from various laser sources is coupled in through the tip, which is brought into contact with the sample. The Ag film on the back of the membrane is 310 nm thick. Slits with widths smaller than 100 nm and lengths of $5 \mu\text{m}$ were made in the back Ag film by focused ion beam milling. Care was taken to stop the milling once the Si₃N₄ layer was exposed. Both single slits and pairs of parallel slits with various separations were fabricated. Panels b and c of Figure 1 show scanning electron microscopy (SEM) images of a typical structure with two slits spaced $1 \mu\text{m}$ apart, viewed in cross section and from the back side. The slits serve to scatter SPPs to the far field at the back side of the sample. The scattered radiation is collected by a $50\times$ microscope objective ($\text{NA} = 0.7$) and focused on a $100 \mu\text{m}$ core diameter multimode optical fiber that is led to an APD detector. Two-dimensional near-field images are obtained by scanning the tip, which acts as the local SPP excitation source, with respect to the sample while monitoring the output from one or two fixed exit slits. From polarization measurements of the tip emission in the far field and from near-field scans across circular slits (data not shown), we determined that the tip acts as a highly polarized excitation source, and therefore as a highly directional source of SPPs. Throughout the measurements, the sample orientation is kept such that the slits are oriented normal to the dominant direction of SPP excitation.

Figure 2a shows a near-field intensity image taken with 638 nm excitation light with a single output slit. The slit is located in the middle of the scan area and oriented in the vertical direction. Three observations can be readily made. First, the signal is highly modulated. The period of the modulation is determined to be 300 nm. In similar measurements on metal films without a MIM structure such modulations were not observed.^{14,15} Second, the signal decays as the excitation source is moved away from the output slit. Third, the image is clearly asymmetric with respect to the slit, which at first sight appears surprising given the symmetry of the measurement geometry. As we will show, this asymmetry can be ascribed to a small asymmetry in the shape of the near-field probe.

To explain the signal modulation and decay, we develop the following model. In the sample geometry that includes the thinned Ag cladding layer, two waveguided SPP modes can propagate. These modes arise from the coupling of SPPs on the three metal/dielectric interfaces: the MIM-SPP mode localized predominantly in the Si₃N₄ layer, and a mode that resides mostly in the air outside the sample (termed “air-SPP” from here on). Figure 1d shows the H field profiles of both modes at a free-space wavelength of 638 nm, calculated by finding the poles of the transfer matrix for the layered sample. The optical constants of Ag are taken from ref 16. Judging from the mode profiles, both modes can be excited by the near-field tip, albeit with different excitation probabilities. Both modes also have a fraction of their energy inside the Si₃N₄ layer, so that they can be scattered by the subwavelength slit to the detector. Because the two modes have a clearly different wave vector, their interference at the output slit will produce the oscillating pattern with varying tip–slit distance that is seen in Figure 2a. As a first approximation, the field at the slit as a function of tip distance x can be described in a one-dimensional scalar model as $E(x) = c_{\text{air}}e^{ik_{\text{air}}x} + c_{\text{MIM}}e^{ik_{\text{MIM}}x}$, where k_{air} and k_{MIM} are the complex wave vectors $k = k' + ik''$ of the air-SPP and MIM-SPP modes, respectively. The complex coefficients c_{air} and c_{MIM} include the amplitude and phase with which each mode is excited. They represent the mode amplitude and phase at the depth of the output slit that scatters the light to the detector. The intensity at the slit then becomes

$$I(x) = |c_{\text{air}}|^2 e^{-2k''_{\text{air}}x} + |c_{\text{MIM}}|^2 e^{-2k''_{\text{MIM}}x} + 2|c_{\text{air}}||c_{\text{MIM}}| e^{-(k''_{\text{air}}+k''_{\text{MIM}})x} \cos[(k'_{\text{MIM}} - k'_{\text{air}})x + \Delta\phi] \quad (1)$$

where $\Delta\phi = \arg(c_{\text{MIM}}c_{\text{air}}^*)$ is the phase difference with which the two modes are excited by the tip.

Figure 2b shows the intensity as a function of distance from the slit, obtained by integrating the intensity in Figure 2a along y . The blue curve is a least-squares fit of eq 1 to the data, where the coefficients $|c_{\text{air}}|$ and $|c_{\text{MIM}}|$ and the phase difference $\Delta\phi$ were allowed to differ on either side of the slit. The data within a distance of 250 nm from the slit were not fit, since directly under the tip the field can obviously not be described sufficiently in terms of two waveguided SPP modes only. Figure 2b shows that the model fits the data well. The oscillatory behavior is reproduced very well, and the decay with distance is identical on each side.

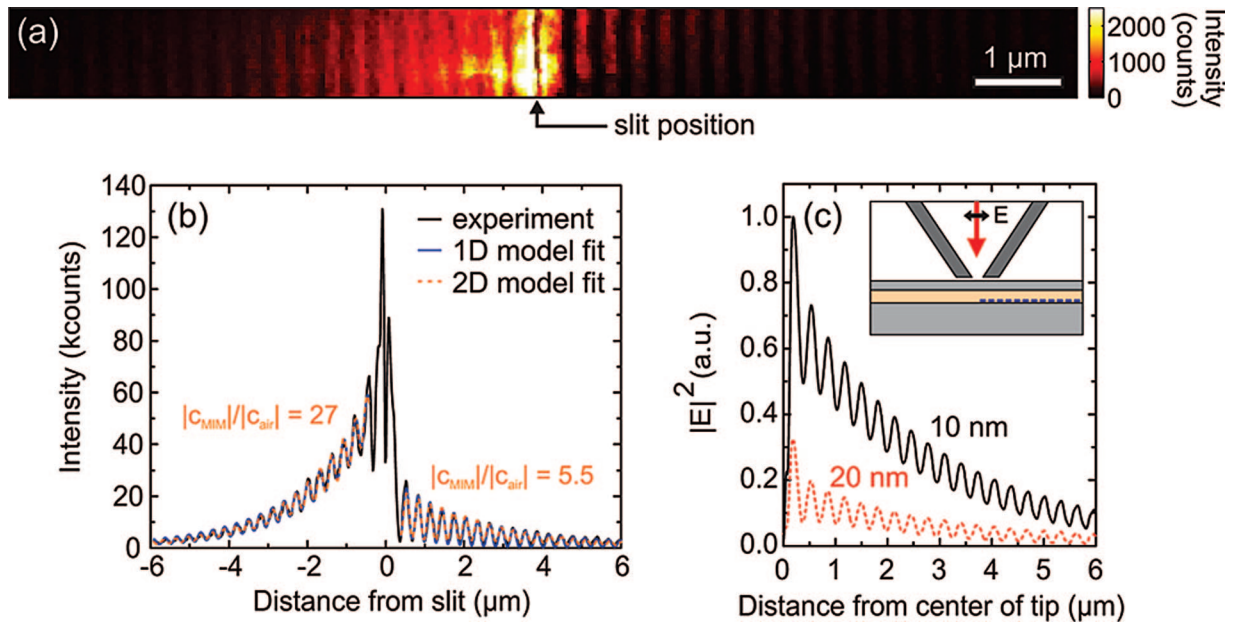


Figure 2. (a) Near-field image obtained by scanning the excitation tip position over the sample containing a single output slit. The excitation wavelength is 638 nm. (b) Collected intensity in panel a as a function of tip–slit distance (black curve), and a fit to the data of the one- and two-dimensional models described in the text (blue and orange curves, respectively). The ratio of the amplitudes of both modes in the two-dimensional model is indicated. (c) Simulated electric field intensity in the Si_3N_4 film as a function of distance from the center of the tip. The inset shows a schematic of the simulated two-dimensional geometry. The dashed blue line indicates the position at which the calculated intensity is plotted. The tip–sample separation is 10 nm (black) or 20 nm (red).

The asymmetry is the result of a difference between the amplitude coefficients at either side of the slit. To understand how the excitability of the modes at opposite sides of the slits can be so different, we performed finite-difference time-domain (FDTD) simulations of the experimental geometry.¹⁷ The geometry of the calculation is sketched in the inset of Figure 2c. The structure is modeled to be invariant in one dimension. The mesh size is 1 nm in the vicinity of the sample and 3 nm further away from it. A p-polarized Gaussian beam with a free-space wavelength of 638 nm is incident through the tip. The output slit is absent in the simulations. The calculated electric field intensity at the bottom side of the Si_3N_4 layer is plotted in Figure 2c for two different separation heights between the tip and the sample. Assuming that the slit acts as a point scatterer, the intensity in this plane can be directly related to the measured signal collected through the slit.

The calculations reveal interference patterns with a period and decay similar to the experiment in Figure 2b. For the 10 nm tip-to-sample separation, the overall intensity is larger and the visibility of the fringes is smaller than those for the 20 nm tip-to-sample separation. For small separations, the Al sidewalls hinder the excitation of the air-SPP.¹⁸ On the other hand, more power is coupled into the MIM-SPP when the distance between tip and sample is reduced. Although during the experiment the tip is in contact with the sample surface, small imperfections in the tip can easily result in different local separations between tip and sample at different sides of the tip. As a result, the asymmetries observed in Figure 2b for the interference pattern on either side of the slit can be ascribed to a small asymmetry in the tip shape. Indeed, when experiments are performed with different tips

on the same sample, different asymmetries are observed that can be explained by changed coefficients c_{MIM} and c_{air} at both sides of the slit. By fitting eq 1 to the data, the difference of the real part of the wave vectors of the two SPP modes is obtained. From the fit we find $\Delta k' = (k'_{\text{MIM}} - k'_{\text{air}}) = 20.69 \mu\text{m}^{-1}$.

This simple one-dimensional model ignores the fact that SPP waves excited by the near-field tip will diverge on the two-dimensional sample surface and that SPPs emitted in different directions travel different distances to the output slit. For this reason, it may be important to consider the resultant field distribution along the length of the slit and the way this distribution is imaged on the detector. To account for the SPP divergence, we construct a two-dimensional model that assumes the tip acts as a polarized point source of SPPs as mentioned above, emitting a field

$$E(r, \theta) = (c_{\text{air}} e^{ik_{\text{air}}r} + c_{\text{MIM}} e^{ik_{\text{MIM}}r}) \frac{\cos(\theta)}{r^{1/2}} \quad (2)$$

where r is the distance to the tip and θ is the angle with respect to the normal of the output slit. To predict the detected intensity as a function of the distance x between tip and slit, the field distribution along the slit is obtained from eq 2. A scalar amplitude point spread function is subsequently used to calculate the field in the image plane of the microscope, and the intensity in this plane is integrated over the area of the fiber core. A resulting fit of this two-dimensional model to the data is shown in Figure 2b as an orange dashed curve. This model also fits the data well, yielding $\Delta k' = 20.43 \mu\text{m}^{-1}$. The fitted propagation length $L \equiv 1/(2k')$ of the MIM-SPP mode is $1.4 \mu\text{m}$, which is smaller than the value of $2.6 \mu\text{m}$ obtained from the mode calculation. We ascribe this discrepancy to a deviation of the actual

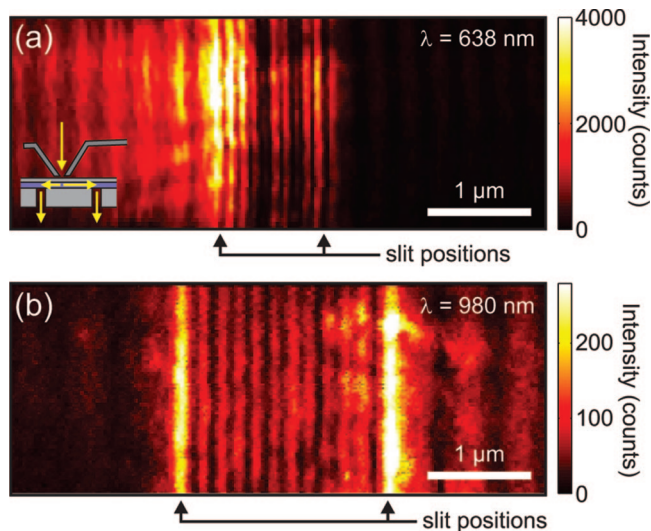


Figure 3. (a) Near-field image obtained by scanning the excitation tip position over the sample containing a pair of output slits separated by $1 \mu\text{m}$. Excitation wavelength is 638 nm. The inset shows the interference mechanism leading to the fast spatial intensity oscillations between the slit. (b) Near-field image as in (a) but for an excitation wavelength of 980 nm and a slit separation of $2 \mu\text{m}$.

optical constants to those used in the calculation and additional scattering losses. The fact that the obtained value of $\Delta k'$ for the one-dimensional model is so close to that obtained with the two-dimensional model shows that a fit of the simple one-dimensional model to the data already yields accurate estimations of the real part of the wave vector. Nevertheless, in the remainder of the analysis, the more accurate two-dimensional model is used.

To determine absolute values of the wavelengths of both SPP modes in addition to the differential wave vector magnitude $\Delta k'$, we performed experiments on pairs of aligned slits separated by micrometer-scale distances. The collection objective is positioned such that light from both slits is simultaneously collected at the same time. When the tip is scanned outside both slits, a similar interference pattern is expected as for the single slit. However, for a tip position between the two slits, a different interference mechanism is expected to come into play, depicted in the inset of Figure 3a. Because the light originating from the two slits will interfere on the detection fiber, a change of the relative phase of the field at the two slits will alter the detected intensity. MIM-SPP waves excited between the slits in opposite directions will arrive at the two slits with a relative phase difference that depends on the position of the excitation source. Because the difference between the two path lengths scales linearly with twice the distance to one of the slits, an interference pattern with a period of half the MIM-SPP wavelength should appear as the tip scans between the slits. The double-slit geometry also produces a pattern with a period of half the air-SPP wavelength. The single slit experiments showed that the contribution of MIM-SPPs to the output signal is larger than that of air-SPPs. Accordingly, the pattern due to MIM-SPP interference can be discerned with respect to the air-SPP pattern, provided that the slit

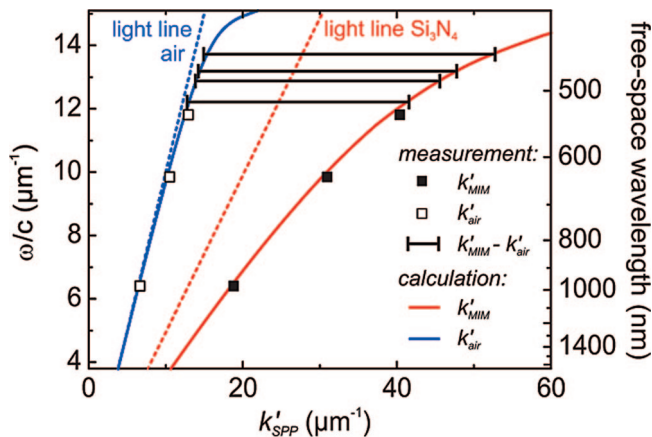


Figure 4. Dispersion relations of the two SPP modes that are supported by the system. Closed and open symbols indicate the measured values of k'_{MIM} and k'_{air} , respectively. The length of the horizontal bars at high frequencies is equal to the experimentally determined values of $(k'_{\text{MIM}} - k'_{\text{air}})$. The solid blue and red lines are the calculated dispersion curves for the air- and MIM-SPP modes, respectively.

separation is not much larger than the MIM-SPP propagation length.

Figure 3a shows the measured near-field image for 638 nm excitation wavelength and a slit separation of $1 \mu\text{m}$. Between the slits an oscillatory pattern with a period of 102 nm is observed. This interference pattern is superimposed on the pattern that was also observed for the single slit and that is also present outside the pair of slits.

Experiments for single slits and pairs of slits are repeated for various excitation wavelengths between 458 and 980 nm. Figure 3b shows an image taken with a pair of slits with a separation of $2 \mu\text{m}$ taken at 980 nm. Clearly an interference pattern is again observed between the slits, with a larger period than that shown in Figure 3a. Because the interference patterns for single slit and double slit experiments provide independent measurements of k'_{MIM} and $\Delta k'$ at each frequency, we can construct dispersion curves for both the MIM-SPP and the air-SPP modes. The results are plotted in Figure 4. The dispersion of light in air and in Si_3N_4 is plotted for reference (dashed lines). For an excitation wavelength of 532 nm, the measured MIM-SPP wavelength is 156 nm, corresponding to a wave vector that is 1.7 times larger than that of light in Si_3N_4 . In stark contrast, the dispersion of the air-SPP mode follows the light line in air closely. The solid curves are the calculated dispersion curves for both modes in the multilayer waveguide geometry. The experimentally determined wave vectors show excellent agreement with these calculations. For wavelengths shorter than 532 nm, it was not possible to accurately determine the value of k'_{MIM} independently, because of limited spatial resolution. For these excitation wavelengths, bars are denoted that show the measured magnitude of $\Delta k'$, which corresponds well with calculations up to the shortest wavelength of 456 nm used in the experiment. These measurements show that the MIM-SPP mode can be probed with the near-field method throughout the visible and near-infrared frequency regimes. The propagation lengths are of the order of micrometers—long

enough to perform interferometric measurements of wave vector differences.

In conclusion, we have demonstrated the direct imaging of MIM-SPPs with subwavelength resolution using a near-field probe, despite the buried nature of these highly confined waves. Interference of MIM-SPPs with air-SPP modes allows the determination of the local wave vector and provides insight into the relative excitation efficiency of both modes. Accurate knowledge of MIM-SPP wave vectors and dispersion is essential for the development of subwavelength components and devices based on MIM geometries. Such components benefit from the ultrasmall mode size and high local fields of MIM-SPPs and may form the basis for future highly integrated photonic circuits. This work provides the means to investigate such nanostructures in detail.

Acknowledgment. The authors would like to thank A. F. Koenderink and H. Zeijlemaker for technical assistance. This work was made possible by the fabrication and characterization facilities of the Amsterdam nanoCenter. It is part of the Joint Solar Programme (JSP) of the Stichting voor Fundamenteel Onderzoek der Materie (FOM), which is financially supported by the Nederlandse organisatie voor Wetenschappelijk Onderzoek (NWO). The JSP is cofinanced by gebied Chemische Wetenschappen of NWO and Stichting Shell Research. Work at Caltech is financially supported by the Air Force Office of Scientific Research, MURI Grant No. FA9550-04-1-0434. J.A.D. gratefully acknowledges fellow-

ship support from the Department of Defense Army Research Office and the National Science Foundation.

References

- (1) Barnes, W. L.; Dereux, A.; Ebbesen, T. W. *Nature* **2003**, *424*, 824–830.
- (2) Ozbay, E. *Science* **2006**, *311*, 189–193.
- (3) Economou, E. N. *Phys. Rev.* **1969**, *182*, 539–554.
- (4) Dionne, J. A.; Sweatlock, L. A.; Polman, A.; Atwater, H. A. *Phys. Rev. B* **2006**, *73*, 035407.
- (5) Zia, R.; Selker, M. D.; Catrysse, P. B.; Brongersma, M. L. *J. Opt. Soc. Am. A* **2004**, *21*, 2442–2446.
- (6) Dionne, J. A.; Lezec, H. J.; Atwater, H. A. *Nano Lett.* **2006**, *6*, 1928–1932.
- (7) Miyazaki, H. T.; Kurokawa, Y. *Phys. Rev. Lett.* **2006**, *96*, 097401.
- (8) Maier, S. A. *Opt. Quantum Electron.* **2006**, *38*, 257–267.
- (9) Berini, P. *Opt. Express* **2006**, *14*, 13030–13042.
- (10) Porto, J. A.; García-Vidal, F. J.; Pendry, J. B. *Phys. Rev. Lett.* **1999**, *83*, 2845–2848.
- (11) Bozhevolnyi, S. I.; Volkov, V. S.; Devaux, E.; Laluet, J.-Y.; Ebbesen, T. W. *Nature* **2006**, *440*, 508–511.
- (12) Pile, D. F. P.; Ogawa, T.; Gramotnev, D. K.; Matsuzaki, Y. *Appl. Phys. Lett.* **2005**, *87*, 261114.
- (13) Lezec, H. J.; Dionne, J. A.; Atwater, H. A. *Science* **2007**, *316*, 430–432.
- (14) Sönnichsen, C.; Duch, A. C.; Steininger, G.; Koch, M.; von Plessen, G.; Feldmann, J. *Appl. Phys. Lett.* **2000**, *76*, 140–142.
- (15) Kwak, E.-S.; Henzie, J.; Chang, S.-H.; Gray, S. K.; Schatz, G. C.; Odom, T. W. *Nano Lett.* **2005**, *5*, 1963–1967.
- (16) Johnson, P. B.; Christy, R. W. *Phys. Rev. B* **1972**, *6*, 4370–4379.
- (17) Lumerical FDTD Solutions 5.0.
- (18) Hecht, B.; Bielefeldt, H.; Novotny, L.; Inoué, Y.; Pohl, D. W. *Phys. Rev. Lett.* **1996**, *77*, 1889–1892.

NL801781G